1   # The North American ASTER Land Surface Emissivity

2   # Database (NAALSED) Version 2.0

3

4   Glynn C. Hulley, Simon J. Hook

5   Jet Propulsion Laboratory, California Institute of Technology, Pasadena, CA, USA

6   G.C. Hulley, Jet Propulsion Laboratory, 4800 Oak Grove Dr, Pasadena, CA, 91109.

7   glynn.hulley@jpl.nasa.gov

9

10   *Abstract*

11   Thermal Infrared (TIR) data are supplied by instruments on several satellite

12   platforms including the Advanced Spaceborne Thermal Emission and Reflection

13   radiometer (ASTER), which was launched on the Terra satellite in 1999. ASTER has five

14   bands in the TIR and a spatial resolution of 90 m. A mean seasonal, gridded, Land

15   Surface Temperature and Emissivity (LST&E) database has been produced at 100 m

16   spatial resolution using all the ASTER scenes acquired for the months of Jan-Mar

17   (winter) and Jul-Sep (summer) over North America. Version 2.0 of the North American

18   ASTER Land Surface Database (NAALSED) (http://emissivity.jpl.nasa.gov) has now

19   been released and includes two key refinements designed to improve the accuracy of

20   emissivities over water bodies and account for the effects of fractional vegetation cover.

21   The water adjustment replaces ASTER emissivity values over inland water bodies with a

22   measured library emissivity spectrum of distilled water, and then re-calculates the surface

23   temperatures using a split-window algorithm. The accuracy of ASTER emissivities over

24   vegetated surfaces is improved by applying a fractional vegetation cover adjustment

25   (TES_Pv) to the ASTER Temperature Emissivity Separation (TES) calibration curve.

26   Comparisons of NAALSED emissivity spectra with in-situ data measured over a

27   grassland in Northern Texas resulted in a combined absolute difference for all five

28   ASTER bands of 1.0 % for the summer emissivity data, and 0.1% for the winter data - a

29   33-50 % improvement over the original TES results.

30

31   **1. INTRODUCTION**

32

33   The emissivity of an isothermal, homogeneous emitter is defined as the ratio of

34   the actual emitted radiance to the radiance emitted from a black body at the same

35   thermodynamic temperature (Norman and Becker 1995). Land Surface Emissivity (LSE)

36   is an intrinsic property of the Earth's surface and is independent of the Land Surface

37   Temperature (LST) which varies with irradiance history and local atmospheric

38   conditions. The emissivity of most natural Earth surfaces for the wavelength range

39   covered by the five ASTER TIR bands between 8-12 μm (Table 1) is from ~0.65 to close

40   to 1.0. Narrowband emissivities less than 0.85 are typical for most desert and semi-arid

41 areas due to the strong quartz absorption feature (reststrahlen band) between 8-9.5 μm

42 range, whereas the emissivity of vegetation, water and ice cover are generally greater

43 than 0.95 and spectrally flat in the 8-12 μm range.

44   Land Surface Temperature and Emissivity (LST&E) data are key parameters in

45 global climate change studies that involve climate modeling, surface-atmosphere

46 interactions and land surface temperature modeling. In land surface temperature

47 modeling, knowledge of the surface emissivity is critical for accurately recovering the

48 LST, a key climate variable in many scientific studies from climatology to hydrology and

49 modeling the greenhouse effect. By inverting the Planck function and simulating a

50 radiative transfer method for estimating LST, it can be shown that an emissivity error of

51 0.005 (0.5%) corresponds to a surface temperature error of ~0.3 K for a material at 300 K

52 and a wavelength of 11 μm. The impact of emissivity errors on LST is larger for split-

53 window algorithms, and depending on the water vapor content, are on average ~0.7 K for

54 a band emissivity uncertainty of 0.005 (0.5%) (Galve et al. 2008).

55   Using the standard ASTER LST&E products (AST_05, AST_08) produced by the

56 ASTER Temperature Emissivity Separation (TES) algorithm (Gillespie et al. 1998), a

57 mean, seasonal, gridded ASTER LST&E dataset has been produced using all ASTER

58 scenes acquired from 2000-2008 for the wintertime (Jan-Mar) and summertime (Jul-Aug)

59 periods over North America - termed the North American ASTER Land Surface

60 Emissivity Database (NAALSED) (Hulley and Hook, 2008; Hulley et al., 2008).

61   Two parameter changes were made to the ASTER TES algorithm on August 1st,

62 2007, first described in Gustafson et al. (2006). The first parameter change removed a

63   threshold classifier which assigned a value of $\varepsilon_{min} = 0.983$ when the spectral contrast, or

64   Minimum-Maximum Difference (MMD) in emissivity was smaller than 0.03 for

65   graybody surfaces (eg. water, vegetation). This change was made to remove artificial step

66   discontinuities in emissivity between vegetated and arid areas. The threshold classifier

67   was initially introduced for graybodies since the MMD for graybody surfaces is

68   dominated by residual sensor noise or the atmospheric correction and frequently does not

69   allow the actual emissivity to be accurately recovered (Gillespie et al. 1998). The

70   consequence of removing the threshold classifier was a smoother appearance for all

71   images, but at the cost of TES underestimating the emissivity of graybody scenes such as

72   water by up to 3%, and vegetation by up to 2% (Hulley et al. 2008). The second

73   parameter change removed the iterative correction for reflected downwelling radiation

74   which also frequently failed due to inaccurate atmospheric corrections (Gustafson et al.

75   2006). Using only the first iteration resulted in improved spectral shape and performance

76   of TES.

77   We describe two adjustments implemented in NAALSED version 2.0 to

78   overcome the problems in TES emissivity and temperature retrievals over graybody

79   surfaces such as water and partially vegetated surfaces. The first adjustment uses a Land-

80   Water Map (LWM) generated from ASTER visible data to replace the TES emissivity of

81   water pixels with the measured emissivity of water from the ASTER Spectral Library

82   (ASL) (Baldridge et al. 2009) and calculating a new temperature for the pixel using a

83   split-window algorithm (Matsunaga 1996). The second adjustment uses a modified TES

84 calibration curve based on fractional vegetation cover to adjust for the effect of mixed

85 pixels of vegetation and other materials.

86

87 **2. ASTER**

88

89 **2.1 Instrument Specifications**

90

91 The Advanced Spaceborne Thermal Emission and Reflection radiometer

92 (ASTER) was launched on the Terra satellite in 1999. ASTER includes 14 spectral bands

93 in three instrument subsystems: the visible and near infrared (VNIR), the short-wave

94 infrared (SWIR), and the thermal infrared (TIR). The TIR subsystem consists of five

95 spectral bands (bands 10-14), with a spatial resolution of 90 m, and is the focus of this

96 study. The radiometric accuracy at 300 K is 1K, and radiometric precision is $\leq 0.3\ K$ at

97 300 K (Fujisada and Ono, 1993). Table 1 gives the spectral range and effective

98 wavelength for each band in the TIR subsystem.

99

100 **2.2 Temperature and Emissivity Separation (TES) Algorithm**

101

102 The ASTER Temperature Emissivity Separation (TES) algorithm is described in

103 Gillespie et al. (1998) and Gustafson et al. (2006). The Gustafson paper describes some

104 recent adjustments to the algorithm. TES is applied to the land-leaving TIR radiances that

105 are estimated by atmospherically correcting the at-sensor radiance on a pixel-by-pixel

106   basis using the MODTRAN radiative transfer code (Kneizys et al. 1996). TES uses an

107   empirical relationship to predict the minimum emissivity (ε_{min}) that would be observed

108   from a given spectral contrast, or Minimum-Maximum Difference (MMD) (Kealy and

109   Hook 1993; Matsunaga 1994). The empirical relationship is referred to as the "calibration

110   curve" and is derived from a subset of spectra in the ASL. TES has been shown to

111   accurately recover temperatures within 1.5 K and emissivities within 0.015 for a wide

112   range of surfaces (Gillespie et al. 1998).

113

114   **3. NAALSED v2.0**

115

116   Using the results from TES, a mean seasonal ASTER LST&E database has been

117   produced at 100 m spatial resolution referred to as the North American ASTER Land

118   Surface Emissivity Database (NAALSED). The database can be ordered from

119   http://emissivity.jpl.nasa.gov and covers the winter months of minimum vegetation cover

120   (Jan-Mar) and summer months of maximum vegetation cover (Jul-Sep). Hulley at al.

121   (2008) provide a detailed description of NAALSED (version 1.0) and initial results for

122   California and Nevada, while Hulley and Hook, (2008) describe a new methodology for

123   ASTER cloud screening in NAALSED. In the two seasonal datasets the emissivity is

124   calculated as the average emissivity of all clear-sky pixels for a given location from all

125   scenes acquired in the season over the entire period of acquisition of ASTER data (2000-

126   2008).

127   NAALSED v2.0 has been validated over barren regions with laboratory

128   measurements of sand samples collected at nine pseudo-invariant sand dune sites located

129   in the western/southwestern USA and covering a broad range of surface emissivities in

130   the TIR. Results show the combined mean emissivity difference between NAALSED and

131   the nine validation sites for all five ASTER TIR bands is 0.016 (1.6 %), equivalent to ~1

132   K error in surface temperature for a material at 300 K (Hulley et al. 2009).

133   An example of the mean summer emissivity for band 12 (9.1 µm) for USA and

134   Mexico is shown in Figure 1. The majority of emissivities range from 0.8 to 0.98, with

135   the lowest emissivities occurring over the quartz-rich deserts of southeastern California,

136   the Colorado Plateau, and the Grand Desierto in Mexico. A total of 70,075 ASTER

137   scenes were processed to produce the emissivity database for the area shown in the

138   image.

139   The NAALSED v2.0 product comprises eighteen bands: the mean and standard

140   deviation of the surface emissivity (all five TIR ASTER bands), surface temperature,

141   NDVI (calculated from the visible data), a Land-Water Map (LWM) (also calculated

142   from the visible data), the total yield (number of ASTER observations used for each

143   pixel), and geodetic latitude and longitude.

144   Including the surface temperature product in the database enables users to re-

145   compute the land-leaving radiance, using the mean emissivity and mean surface

146   temperature as inputs, and then apply a decorrelation stretch (d-stretch) algorithm. The d-

147   stretch exploits inter-channel differences to enhance the color in images, resulting in an

148   image where the pixels are distributed among the full range of possible colors, while

149   preserving the saturation and intensity of the input image. D-stretch images are used

150   primarily for geologic and mineral mapping, and resource exploration in which any color

151   variation is due to emissivity differences and any brightness variation is due to

152   temperature differences (Massironi et al. 2008; Rockwell and Hofstra 2008; Vaughan et

153   al. 2005). The principle drawback when using d-stretches is that the algorithm will

154   enhance any noise and processing artifacts in the input image resulting in scene variation

155   being dominated by noise. However, the advantage of using the NAALSED mean

156   emissivity and surface temperature products is they have far less noise than the standard

157   ASTER products due to pixel averaging, resulting in d-stretch images that have much less

158   noise and are easier to interpret. Figure 2 shows four examples of NAALSED d-stretch

159   images using ASTER bands 14, 12, and 10 as red, green and blue (RGB) respectively

160   over the Colorado Plateau, Colorado; Death Valley, California; Organ Pipe Cactus

161   National Park, Mexico; and Cuprite, Nevada. Quartz-rich rocks are displayed in red and

162   magenta, quartz-poor rocks in blues and purples, and carbonates in green. Temperature

163   information is related to the brightness of the images, ie. areas of higher elevation appear

164   darker than lower elevation areas.

165

166   **3.1 Water Adjustment**

167

168   The performance of TES over water was analyzed by looking at all fifty-five

169   ASTER observations acquired over Lake Tahoe, California from 2000-2008. The ASTER

170   mean and temporal variation in emissivity for a pixel centered on the lake (39.15º N, -

171   120º W) were for band 10 (8.3 μm): 0.965 ± 0.008, band 11 (8.6 μm): 0.962 ± 0.008,

172   band 12 (9.1 μm): 0.958 ± 0.009, band 13 (10.6 μm): 0.974 ± 0.004, and band 14 (11.3

173   μm): 0.973 ± 0.003. These means are plotted in Figure 3 along with the emissivity of

174   distilled water from the ASL (http://speclib.jpl.nasa.gov). The results show that TES

175   underestimates the emissivity of water by up to 2.67% in band 12, with mean differences

176   of 2% for all bands, and standard deviations of almost 1% for bands 10-12. These

177   differences are a consequence of the first parameter change to TES as discussed earlier

178   and detailed in Gustafson et al. (2006). Tonooka and Palluconi (2005) showed that an

179   increase in Precipitable Water Vapor (PWV) resulted in larger residual errors in the

180   atmospherically corrected data, which in turn resulted in a larger variance of MMD. It

181   was found that for an atmosphere with a PWV of 3 cm, the residual error resulted in a

182   MMD of 0.049, and a surface temperature error of 2.3 ºC. It should be noted that early

183   ASTER data also included a residual radiometric calibration error which has now been

184   corrected (Hook et al. 2007; Tonooka et al. 2005).

185   In order to avoid the unrealistically low emissivity values over water, we used a

186   high resolution LWM derived from ASTER visible data to distinguish between land and

187   water pixels, and then set the emissivity for water pixels to that of distilled water from the

188   ASL. Figure 4 shows the emissivity comparison between TES and the ASL value for

189   distilled water for band 12 (9.1 μm) over Lake Tahoe and surrounding lakes. All land

190   surface pixels are screened out using the LWM. The LWM is computed using a

191   modification of the Normalized Difference Vegetation Index (NDVI), which takes

192   advantage of water having lower reflectance in the near-infrared (ASTER band 3) than in

193   the visible red (ASTER band 2). However, to increase sensitivity in distinguishing

194   between water and land pixels, we replace the red band with the ASTER green band

195   (band 1). The ASTER NDVI for water is then computed as follows:

196

$$NDVI = \frac{r_3 - r_1}{r_3 + r_1} \qquad (1)$$

197

198   where, r_3 and r_1 are Top Of Atmosphere (TOA) reflectances (Markham and Barker 1986)

199   for ASTER bands 1 and 3 centered on 0.56 and 0.82 μm. The LWM is then computed

200   using a combination of NDVI and r_3 tests. Suitable thresholds were found by computing

201   NDVI and r_3 for a range of values between 0 to 0.1 in increments of 0.005 and

202   combining the results to produce a range of LWM's over Lake Tahoe, Salton Sea, Great

203   Salt Lake and various other smaller reservoirs. As there is currently no water mask at

204   higher resolution than NAALSED (100m) to make comparisons with, we found that

205   generating Google Earth kml files of the LWM's and overlaying the results in Google

206   Earth was a quick and easy way to assess the results of the NAALSED LWM. Through a

207   visual assessment, values of NDVI ≤ 0.05 and r_3 ≤ 0.04 were found to be optimal for

208   discriminating between land and water pixels, independent of the elevation of the water

209   body. In the future, validation with ASTER 90 m reflectance data will be made, and user

210   feedback will be combined to investigate possible problem areas.

211   Additional comparisons were made with a new 250 m Global Land/Water Mask

212   created at the University of Maryland (UMD) (Carroll et al. 2009). Comparisons between

213   the NAALSED generated LWM and UMD LWM are shown in Figure 5 for an area

214   selected around Lake Tahoe, California/Nevada. Both LWM's show very good agreement

215   with each other, although the NAALSED LWM shows more detail in certain areas, while

216   the UMD LWM has a larger number of water pixels on the edges of water bodies due to

217   the lower spatial resolution.

218   Once the water pixels are identified, their emissivities are set to that of distilled

219   water from the ASL and a differential absorption (split-window) algorithm is used to

220   compute the water surface temperature. Temperatures are computed using the ASTER

221   Multi-Channel Sea-Surface Temperature (MCSST) equation which is based on a linear

222   regression analysis for ASTER TIR data, with an RMSE of 0.74 K (Matsunaga 1996).

223   The regression equations and coefficients are optimized by using simulated data derived

224   from a global-based simulation model (Tonooka 2005). The model is generated by using

225   atmospheric profiles derived from the National Center for Environmental Prediction

226   (NCEP) Climate Data Assimilation System (GDAS) for a wide range of different

227   conditions, and combined with MODTRAN 4.2 to derive the at-sensor radiance.

228

229   **3.2 Vegetation Adjustment**

230

231   Previous studies (Coll et al. 2007; Jiménez-Muñoz et al. 2006) noted an

232   inaccuracy in the ASTER emissivities over vegetation and they were able to improve the

233   accuracy using ASTER scenes over a small number of test sites. Jiménez-Muñoz et al.

234   (2006) proposed a method for improving ASTER emissivities over agricultural regions

235 using ASTER NDVI, and Coll et al. (2007) used scene-based adjusted radiances with

236 local radiosonde data to obtain more accurate MMD estimates from TES.

237   The emissivity for most types of green vegetation is high and spectrally flat (low

238 MMD), although grasses tend to have larger MMD's (Salisbury and Daria 1992). We

239 have developed an alternate approach to adjusting the emissivity over vegetated surfaces

240 by computing a new ε_{min} vs MMD regression curve by smoothly varying the emissivity

241 spectra of 59 rock and soil samples from zero to full vegetation cover using a simplified

242 equation for predicting emissivity from NDVI values (Sobrino and Raissouni 2000; Valor

243 and Caselles 1996):

244

$$\varepsilon_b = \varepsilon_b^v \cdot P_v + \varepsilon_b^s \cdot (1 - P_v) \tag{2}$$

245

246 where ε_b^v and ε_b^s are emissivity values for vegetation and bare soil for ASTER band b,

247 and P_v is the fractional vegetation cover. The dataset used consists of spectra from the

248 nine sand dune samples discussed in Hulley et al. (2009), along with 49 soil spectra from

249 the ASL classified in terms of soil taxonomy as Aridisol (14 samples), Alfisol (9

250 samples), Entisol (10 samples), Inceptisol (7 samples) and Mollisol (9 samples). For each

251 of the 59 samples, we compute a full amplitude range in emissivity from a bare to fully

252 vegetated surface by varying the P_v from 0 to 100% in steps of 5% and using the conifer

253 vegetation spectra in the ASL for ε_b^v. The conifer spectra measurement was made at

254 Johns Hopkins University (JHU) and reduced in reflectance by a factor of two to account

255 for canopy scattering effects. Norman et al. (1995) found that the emissivity of canopies

256   normally varies from 0.97 to 0.99, for a leaf emissivity measurement of 0.95. Therefore,

257   the conifer spectra, which has an ε_{min} of 0.989 and MMD of 0.003, gives a good

258   approximation for the effective emissivity of a tree canopy. The spectra were convolved

259   to the ASTER spectral response functions and ε_{min} was found for each sample. The β

260   spectra and corresponding MMD were then calculated for a range of P_v values, and the

261   ε_{min} data were regressed to the MMD values as in Gillespie et al. (1998). The resulting

262   regression curve, termed TES_Pv, is expressed as follows:

263

$$\varepsilon_{min} = 0.9951 - 0.7264 \cdot MMD^{0.7873} \qquad (3)$$

264

265   Figure 6 shows the TES_Pv compared to that of the current TES curve. The right panel

266   shows a subset of the data for ε_{min} values greater than 0.9. From Figure 6, we can see

267   that TES_Pv will result in larger ε_{min} values of up to 1% for a given MMD and ε_{min}

268   values greater than 0.7. The strategy used for incorporating TES_Pv with the TES result

269   is to engage TES_Pv for surfaces with ε_{min} values above 0.949, the highest value of all

270   sand/soil samples in the dataset. All ε_{min} values greater than this are identified as being

271   in the 'vegetation regime', and a new ε_{min} value is computed using (3), which in turn is

272   used to compute an adjusted emissivity spectrum.

273   In order to evaluate TES_Pv, differences with TES were calculated over an area

274   covering three different vegetation types; croplands in the Central Valley, which

275   transition to savanna grasslands further east, and redwood forests in Sequoia National

276   Park. Figure 7 shows spatial variations in emissivity over the Central Valley area using

277   ASTER mean summer emissivities extracted from NAALSED. The contrast in emissivity

278   was first enhanced using histogram-equalization and then plotted using emissivity bands

279   10, 12 and 14 as red, green and blue respectively. Areas of dense forest canopies over

280   Sequoia and Kings Canyon National Park and croplands in the southwest of the image

281   show up as white and light blue in color, whereas grasses and shrubs show up as green

282   and yellow. Low emissivity values in bands 10-12 over bare areas of the Sierras to the

283   east and the city of Fresno in the west appear as dark shades of purple and black.

284   Figure 8 shows comparisons between the emissivity in bands 12 (left panels) and

285   14 (right panels) from the original TES and TES_Pv. The corresponding histogram of the

286   emissivities from the two methods in Figure 9 shows that TES_Pv smoothly increases the

287   emissivity from bare to vegetated areas, with no apparent step discontinuities. The

288   emissivity differences in the bottom panels of Figure 8 range from 0 to 1% in emissivity

289   and Figure 10 shows a histogram of the range in differences for all pixels in the plot.

290   Above zero, the skewness is negative, centered around 0.4%, with maximum differences

291   of between 0.9 and 1% in emissivity.

292

293   **4. VEGETATION VALIDATION**

294

295   Emissivity validation using single leaf reflectance measurements from spectral

296   libraries such as ASL is difficult from the remote sensing point of view because a sensor

297   such as ASTER (90 m spatial resolution) will observe much higher emissivities due to

298   canopy scattering effects (Palluconi et al. 1990). As mentioned earlier, Norman et al.

299   (1995) found that the emissivity of canopies normally varies from 0.97 to 0.99, for a leaf

300   emissivity measurement of 0.95.

301   As a result, we have assessed the NAALSED emissivity spectra over vegetation

302   by comparing the results with in-situ field measurements obtained by using a sun-shadow

303   method over a grassland area (>80% cover) in Dallam County Texas in April 2005 (Wan

304   2008). The surface radiance was measured with a thermal infrared interferometric

305   spectroradiometer, while the downward sky irradiance was measured with a sand-blasted

306   aluminum plate above the surface target. Details of the field measurement setup are given

307   in Wan, (2008). NAALSED summer and wintertime emissivities were extracted for a 10

308   ✕10 pixel (1 km✕1km) area around the measurement site.

309   Figure 11 shows the emissivity spectra comparisons between NAALSED

310   TES_Pv, the original TES, and in-situ data convolved to the appropriate ASTER spectral

311   response functions for summer and winter data. The in-situ emissivity spectra is high

312   (~0.98) and spectrally flat as expected. The NAALSED winter product had one ASTER

313   observation in the Jan-Mar period 2000-2008, while the summer data had four

314   observations in the Jul-Sep period from 2000-2008. Results in Table 2 show the mean

315   differences for all five ASTER TIR bands (bias) and the combined spatial and temporal

316   variation (σ) for the ASTER observations mentioned above. The TES_Pv summertime

317   results had a 33% improvement over TES with biases of -1.0% (TES_Pv) and -1.5 %

318   (TES) while the wintertime differences matched very closely for both methods with

319   biases of -0.2 % for TES and 0.1 % for TES_Pv. The NAALSED spectra have improved

320   spectral shape (flatter) and absolute magnitude (higher) during the winter period when

321   compared to the in-situ data. This can be explained by the larger MOD08 Precipitable

322   Water Vapor (PWV) during the summer (2.37 ± 0.7 cm) when compared to winter (0.35

323   cm) which results larger apparent MMD values in TES (higher spectral contrast) due to

324   errors in the standard atmospheric correction (Tonooka 2005). The mean NDVI over the

325   grassland showed some seasonal variability with higher summertime values (0.29) than

326   wintertime (0.17). We do not expect the NDVI to be well correlated with ASTER

327   emissivity over the grassland due to the multiple scattering effects of persistent plant

328   matter regardless of chlorophyll content (French et al. 2008; Palluconi et al. 1990). The

329   combined standard deviation in emissivity (σ) for both seasons were similar and less than

330   1%, with the spatial standard deviation on the 10×10 km area accounting for most of the

331   variation.

332

333   **5. CONCLUSIONS**

334

335   The North American ASTER Land Surface Emissivity Database (NAALSED)

336   version 2.0 consists of a mean, seasonal, gridded ASTER Land Surface Temperature and

337   Emissivity (LSTE&E) product using all ASTER data acquired from 2000 to 2008.

338   Version 2.0 of NAALSED includes two enhancements to improve the accuracy of the

339   Temperature Emissivity Separation algorithm (TES) retrieved emissivities over graybody

340   surfaces: 1) a water adjustment and 2) the compensation for partially vegetated surfaces.

341   The two enhancements over graybody surfaces were made to compensate for the removal

342   of a threshold classifier in TES, and account for propagation of atmospheric errors which

343   results in TES underestimating the emissivity over water and vegetation from 1-3%.

344   The water adjustment uses an ASTER produced Land-Water Map (LWM) to

345   replace the emissivity of all water pixels in NAALSED with that of the emissivity of

346   distilled water from the ASTER Spectral Library (ASL). This adjustment will account for

347   the ~2% bias in TES retrieved emissivities over water bodies. A new surface temperature

348   is calculated using a split-window technique over water bodies which is reported in

349   NAALSED. The second enhancement used a new calibration curve based on fractional

350   vegetation cover change to estimate the emissivity over partially vegetated surfaces.

351   Applying the new TES_Pv curve to the TES standard emissivity product over Central

352   Valley in California resulted in higher emissivities by on average 0.5%, and up to 1.0%

353   with no change in spectral shape or discontinuities in transition zones from vegetated to

354   bare areas.

355   An assessment of the two methods over vegetation was made by comparing

356   NAALSED emissivity spectra with in-situ data over a grassland in Northern Texas.

357   Results show mean differences of -1.5% (TES) and -1.0 % (TES_Pv) during summer

358   observations and 0.2% (TES) and -0.1% (TES_Pv) during winter observations. The

359   improved winter results were a result of a much drier atmosphere which minimizes

360   atmospheric correction errors in the TES algorithm.

361   NAALSED is the first high resolution (100 m), validated LSTE&E database of

362   its kind, and should prove very valuable to the broad scientific community. Specifically,

363   it can be used as a baseline for validating other LST&E products from sensors with much

364   coarser spatial resolution such as the Moderate Resolution Imaging Spectroradiometer

365   (MODIS; 5 km), the Atmospheric Infrared Sounder (AIRS; 45 km) and future

366   instruments such as the Visible/Infrared Imager Radiometer Suite (VIIRS; MODIS

367   follow-on) and the Cross-track Infrared Sounder (CrIS; AIRS follow-on) on the NPOESS

368   Preparatory Project (NPP). Until now, validation of coarse resolution data has been

369   difficult due to a lack of higher spatial resolution validated data. NAALSED provides

370   both an emissivity mean and standard deviation for a specific location, which can be used

371   as an *a priori* emissivity estimate and an acceptable error-bound in climate model inputs

372   and atmospheric retrieval schemes from other sensors.

373

374   **Acknowledgements.** The research described in this paper was carried out at the Jet

375   Propulsion Laboratory, California Institute of Technology, under the contract with the

376   National Aeronautics and Space Administration. We kindly thank Dr. Zhengming Wan

377   from University of California Santa Barbara for providing the Texas grassland emissivity

378   spectra. ASTER data were provided by the USGS Center for Earth Resources

379   Observation and Science (EROS) in Sioux Falls, South Dakota.

380

381   **References**

382

383   Baldridge, A.M., Hook, S.J., Grove, C.I., & Rivera, G. (2009). The ASTER Spectral

384   Library Version 2.0. *Remote Sensing of Environment, 114,* (4), 711-715

385   Carroll, M., Charlene, D., Townshend, J., Noojipady, P., & Sohlberg, R. (2009). UMD

386   Global 250 meter Land Water Mask User Guide.

387   http://landcover.org/data/guide/technical/techguide_watermask.pdf

388   Coll, C., Caselles, V., Valor, E., Niclos, R., Sanchez, J.M., Galve, J.M., & Mira, M.

389   (2007). Temperature and emissivity separation from ASTER data for low spectral

390   contrast surfaces. *Remote Sensing of Environment, 110,* (2), 162-175

391   French, A.N., Schmugge, T.J., Ritchie, J.C., Hsu, A., Jacob, F., & Ogawa, K. (2008).

392   Detecting land cover change at the Jornada Experimental Range, New Mexico with

393   ASTER emissivities. *Remote Sensing of Environment, 112,* (4), 1730-1748

394   Galve, J.A., Coll, C., Caselles, V., & Valor, E. (2008). An atmospheric radiosounding

395   database for generating land surface temperature algorithms. *Ieee Transactions on*

396   *Geoscience and Remote Sensing, 46,* (5), 1547-1557

397   Gillespie, A., Rokugawa, S., Matsunaga, T., Cothern, J.S., Hook, S., & Kahle, A.B.

398   (1998). A temperature and emissivity separation algorithm for Advanced Spaceborne

399   Thermal Emission and Reflection Radiometer (ASTER) images. *Ieee Transactions on*

400   *Geoscience and Remote Sensing, 36,* (4), 1113-1126

401   Gustafson, W.T., Gillespie, A.R., & Yamada, G.J. (2006). Revisions to the ASTER

402   temperature/emissivity separation algorithm, *2nd International Symposium on Recent*

403   *Advances in Quantitative Remote Sensing*. Torrent (Valencia), Spain

404   Hook, S.J., Vaughan, R.G., Tonooka, H., & Schladow, S.G. (2007). Absolute radiometric

405   in-flight validation of mid infrared and thermal infrared data from ASTER and MODIS

406   on the terra spacecraft using the Lake Tahoe, CA/NV, USA, automated validation site.

407   *Ieee Transactions on Geoscience and Remote Sensing, 45,* (6), 1798-1807

408   Hulley, G.C., & Hook, S.J. (2008). A new methodology for cloud detection and

409   classification with ASTER data. *Geophysical Research Letters, 35,* (16), L16812, doi:

410   16810.11029/12008gl034644

411   Hulley, G.C., Hook, S.J., & Baldridge, A.M. (2008). ASTER land surface emissivity

412   database of California and Nevada. *Geophysical Research Letters, 35,* (13), L13401, doi:

413   13410.11029/12008gl034507

414   Hulley, G.C., Hook, S.J., & Baldridge, A.M. (2009). Validation of the North American

415   ASTER Land Surface Emissivity Database (NAALSED) Version 2.0 using Pseudo-

416   Invariant Sand Dune Sites. *Remote Sensing of Environment*, In review

417   Jiménez-Muñoz, J.C., Sobrino, J.A., Gillespie, A., Sabol, D., & Gustafson, W.T. (2006).

418   Improved land surface emissivities over agricultural areas using ASTER NDVI. *Remote*

419   *Sensing of Environment, 103,* (4), 474-487

420   Kealy, P.S., & Hook, S. (1993). Separating temperature & emissivity in thermal infrared

421   multispectral scanner data: Implication for recovering land surface temperatures. *Ieee*

422   *Transactions on Geoscience and Remote Sensing, 31,* (6), 1155-1164

423   Kneizys, F.X., Abreu, L.W., Anderson, G.P., Chetwynd, J.H., Shettle, E.P., Berk, A.,

424   Bernstein, L.S., Robertson, D.C., Acharya, P.K., Rothman, L.A., Selby, J.E.A., Gallery,

425   W.O., & Clough, S.A. (1996). The MODTRAN 2/3 Report & LOWTRAN 7 Model,

426   F19628-91-C-0132. P. Lab. (Ed.). Hanscom AFB, MA

427   Markham, B.L., & Barker, J.L. (1986). Landsat MSS & TM Post-Calibration Dynamic

428   Ranges, Exoatmospheric Reflectances & At-Satellite Temperatures, *EOSAT Landsat*

429   *Technical Notes, No. 1.*

430   Massironi, M., Bertoldi, L., Calafa, P., Visona, D., Bistacchi, A., Giardino, C., &

431   Schiavo, A. (2008). Interpretation and processing of ASTER data for geological mapping

432   and granitoids detection in the Saghro massif (eastern Anti-Atlas, Morocco). *Geosphere,*

433   *4,* (4), 736-759

434   Matsunaga, T. (1994). A temperature-emissivity separation method using an empirical

435   relationship between the mean, the maximum, & the minimum of the thermal infrared

436   emissivity spectrum, in Japanese with English abstract. *Journal Remote Sensing Society*

437   *Japan, 14,* (2), 230-241

438   Matsunaga, T. (1996). Water Temperature Estimation Based on Linear Regression

439   Analysis for ASTER/TIR. *Journal Remote Sensing Society Japan, 16,* (5), 2-13

440   Norman, J.M., & Becker, F. (1995). Terminology in Thermal Infrared Remote-Sensing of

441   Natural Surfaces. *Agricultural and Forest Meteorology, 77,* (3-4), 153-166

442   Palluconi, F., Kahle, A.B., Hoover, G., & Conel, J.E. (1990). The spectral emissivity of

443   prairie & pasture grasses at Konza Prairie, Kansas, *In Proc. of the Amer. Meteorol. Soc.*

444   *Symposium on the First ISLSCP Field Experiment (FIFE)* (pp. 77-78): American

445   Meteorological Society

446   Rockwell, B.W., & Hofstra, A.H. (2008). Identification of quartz and carbonate minerals

447   across northern Nevada using ASTER thermal infrared emissivity data - Implications for

448   geologic mapping and mineral resource investigations in well-studied and frontier areas.

449   *Geosphere, 4,* (1), 218-246

450   Salisbury, J.W., & Daria, D.M. (1992). Emissivity of Terrestrial Materials in the 8-14

451   Mu-M Atmospheric Window. *Remote Sensing of Environment, 42,* (2), 83-106

452   Sobrino, J.A., & Raissouni, N. (2000). Toward remote sensing methods for land cover

453   dynamic monitoring: application to Morocco. *International Journal of Remote Sensing,*

454   *21,* (2), 353-366

455   Tonooka, H. (2005). Accurate atmospheric correction of ASTER thermal infrared

456   imagery using the WVS method. *Ieee Transactions on Geoscience and Remote Sensing,*

457   *43,* (12), 2778-2792

458   Tonooka, H., & Palluconi, F.D. (2005). Validation of ASTER/TIR standard atmospheric

459   correction using water surfaces. *Ieee Transactions on Geoscience and Remote Sensing,*

460   *43,* (12), 2769-2777

461   Tonooka, H., Palluconi, F.D., Hook, S.J., & Matsunaga, T. (2005). Vicarious calibration

462   of ASTER thermal infrared bands. *Ieee Transactions on Geoscience and Remote Sensing,*

463   *43,* (12), 2733-2746

464   Valor, E., & Caselles, V. (1996). Mapping land surface emissivity from NDVI:

465   Application to European, African, and South American areas. *Remote Sensing of*

466   *Environment, 57,* (3), 167-184

467   Vaughan, R.G., Hook, S.J., Calvin, W.M., & Taranik, J.V. (2005). Surface mineral

468   mapping at Steamboat Springs, Nevada, USA, with multi-wavelength thermal infrared

469   images. *Remote Sensing of Environment, 99,* (1-2), 140-158

470   Wan, Z.M. (2008). New refinements and validation of the MODIS Land-Surface

471   Temperature/Emissivity products. *Remote Sensing of Environment, 112,* (1), 59-74

472
473

474   Table 1. ASTER effective wavelength (λ_{eff}) and spectral range ($\Delta\lambda$) for bands 10-14.

ASTER Band	λ_{eff}(µm)	$\Delta\lambda$ (µm)
10	8.3	8.125 - 8.475
11	8.65	8.475 - 8.825
12	9.1	8.925 - 9.275
13	10.6	10.25 - 10.95
14	11.3	10.95 - 11.65

475

476

477   Table 2. Seasonal emissivity differences between NAALSED TES_Pv, TES, and in-situ

478   data from a grassland in Northern Texas, and differences between TES and the ASL

479   spectra of distilled water. The bias gives the mean differences for all five ASTER TIR

480   bands (Table 1), and σ gives the mean combined spatial and temporal variation of the

481   ASTER data for a 10×10 pixel (1 km×1km) area over the validation site. The mean

482   NDVI (from NAALSED) and MODIS (MOD08) Total Precipitable Water Vapor (PWV)

483   estimates are also shown as reference.

Surface	Season	Method	NDVI	PWV (cm)	Bias (%)	σ(%)
Grassland	Summer	TES	0.29	2.37 ± 0.7	-1.45	0.7
		TES_Pv	0.29	2.37 ± 0.7	-1.04	0.7
	Winter	TES	0.17	0.35	-0.19	0.9
		TES_Pv	0.17	0.35	0.05	0.9
Water	Annual	TES	n/a	n/a	-2.01	0.6
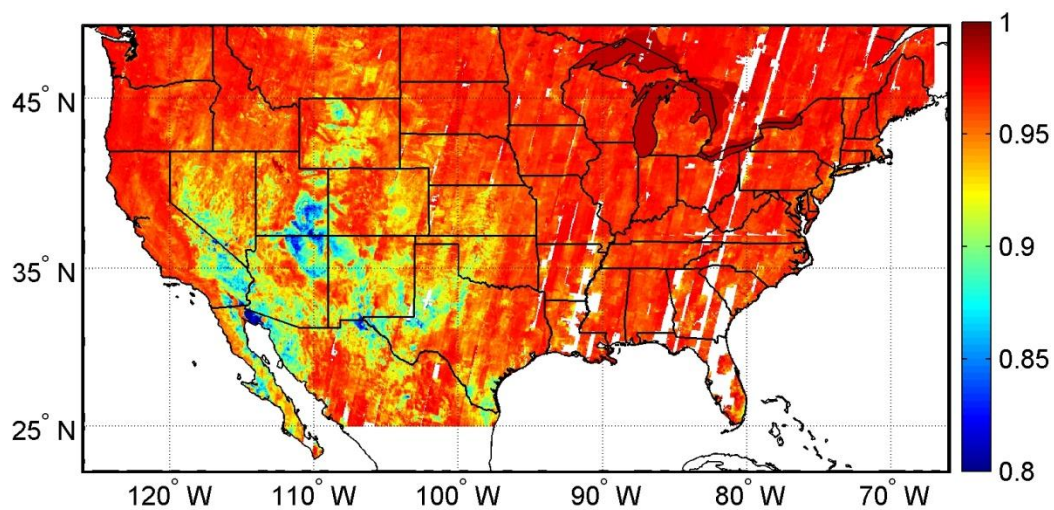
Figure 1. NAALSED mean Summer (Jul-Sep) emissivity for band 12 (9.1 μm) using 70, 075 ASTER scenes acquired from 2000-2008. White areas over land had no clear sky coverage and plan to be filled during the 2009 Summer acquisition period.
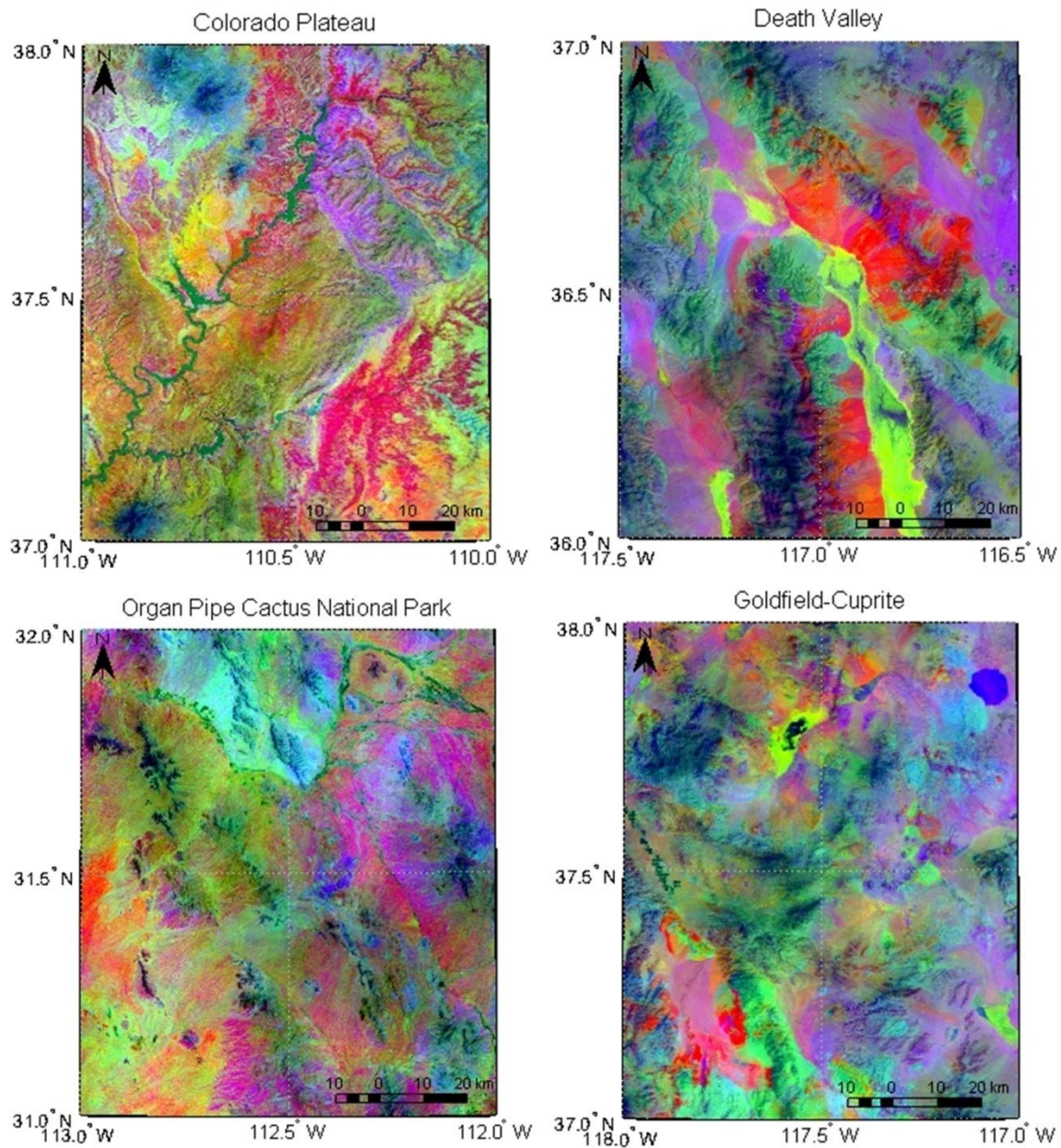
Figure 2. NAALSED decorrelation stretch images using ASTER bands 14, 12, and 10 displayed as red, green and blue respectively over the Colorado Plateau, Colorado; Death Valley, California; Organ Pipe Cactus National Park, Mexico; and Cuprite, Nevada. Quartz rich rocks are displayed in red and magenta, quartz-poor rocks in blues and purples, and carbonates in green.

495
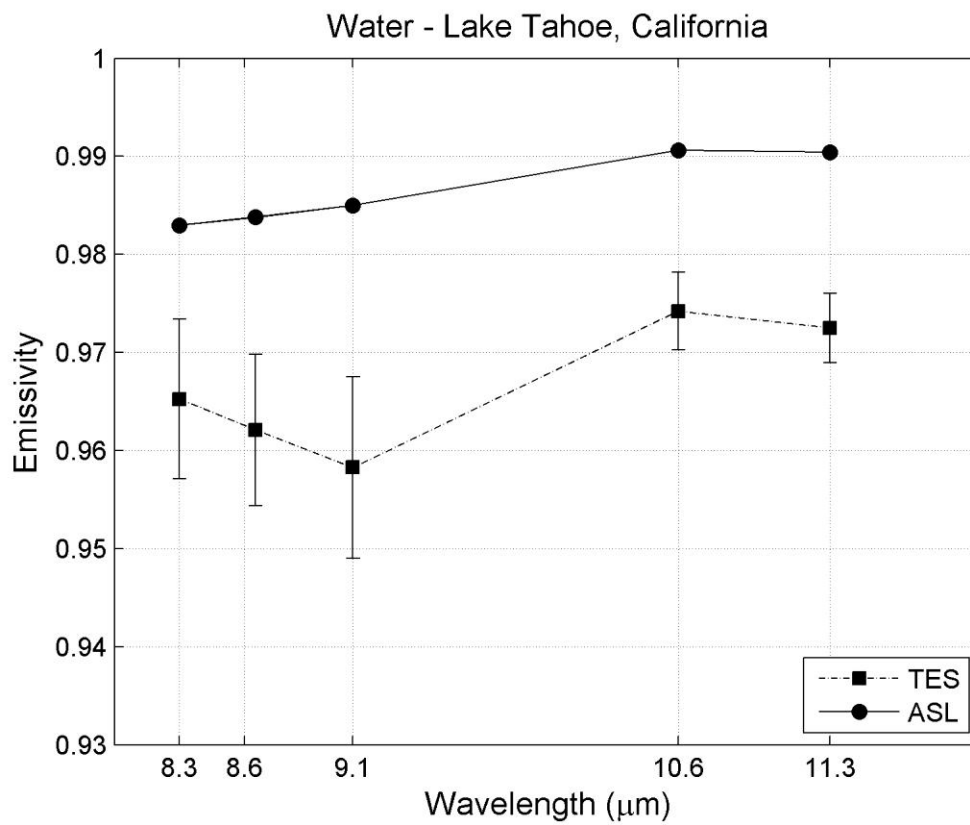
496

497   Figure 3. Comparisons of emissivity spectra between the ASTER spectral library for

498   water, and ASTER data for all clear-sky scenes acquired over Lake Tahoe from 2000-

499   2008. Error bars show the mean and standard deviation in emissivity for all ASTER

500   observations.

501

502
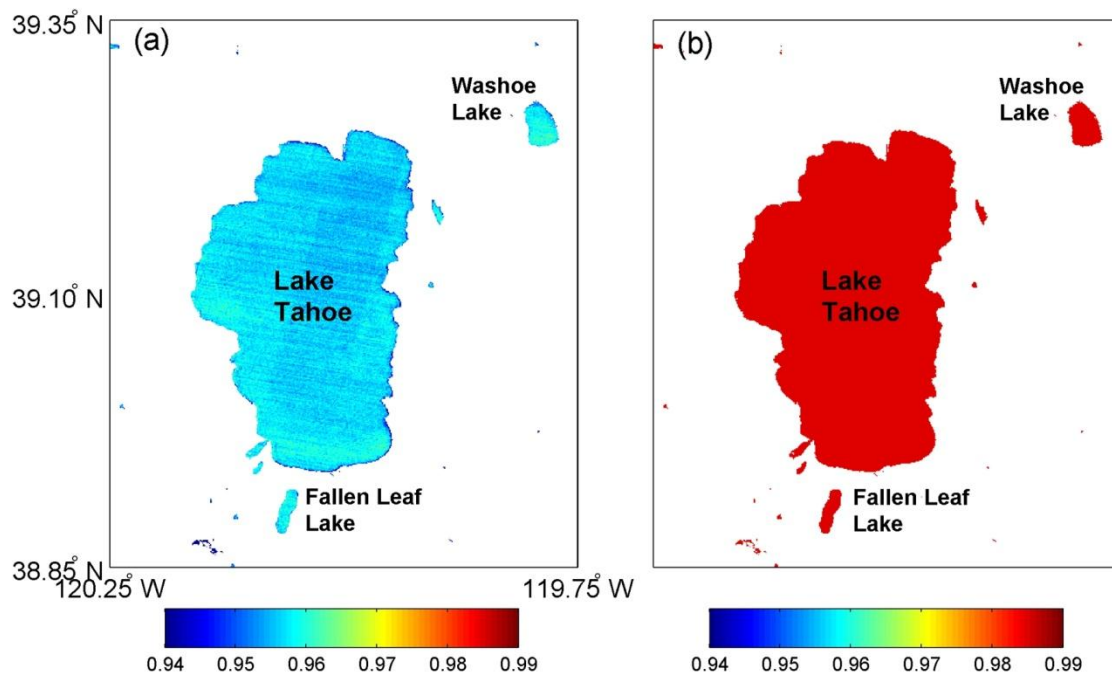
Figure 4. Emissivity comparisons between (a) TES and (b) the emissivity of distilled water from the ASTER spectral library for band 12 (9.1 µm) over Lake Tahoe and surrounding lakes. All land surface pixels have been set to white space using the Land-Water Map (LWM) from NAALSED.

UMD 250 m LWM   NAALSED 100 m LWM
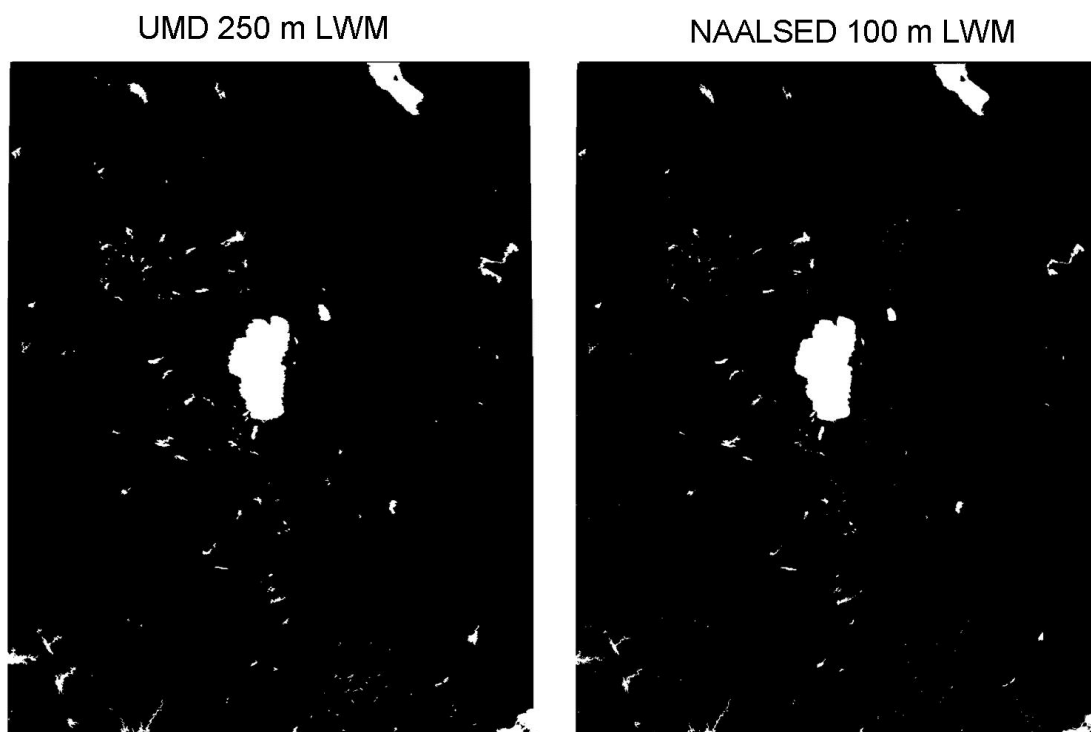
Figure 5. Land-Water Map (LWM) comparisons between the new UMD 250 m LWM (left) and the NAALSED 100 m LWM (right) with Lake Tahoe, California/Nevada at center. White pixels represents water, and black represents land.

514
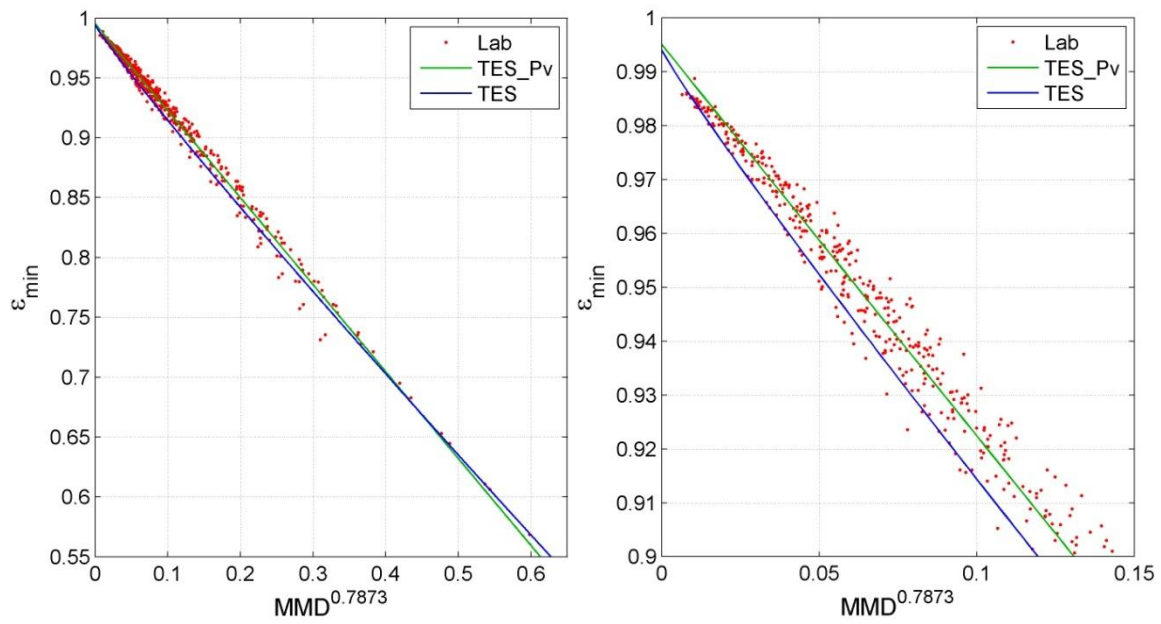
515   Figure 6. Empirical relationship between ε_{min} and MMD for the current TES curve

516   (blue) and TES_Pv (green) for 59 soil and sand spectra from the ASTER spectral library.

517   The right panel shows a subset of results for emissivities greater than 0.9.

518

519
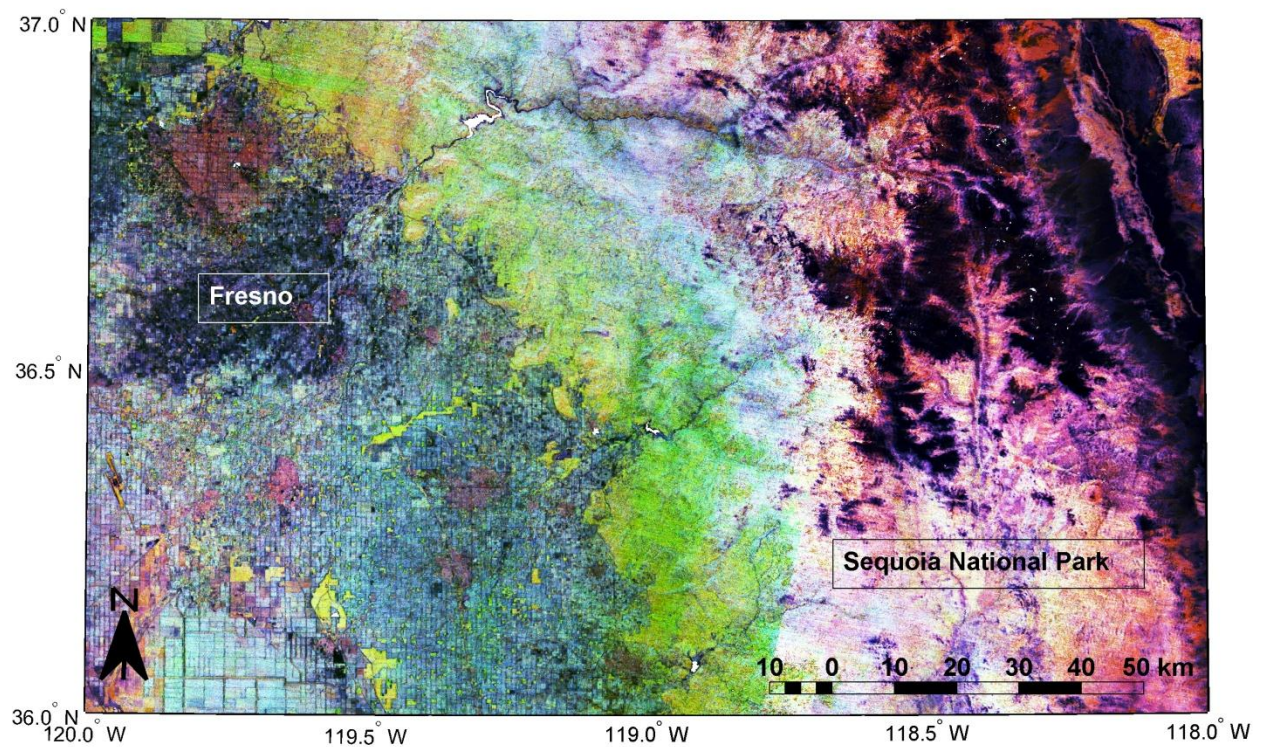
520   Figure 7. NAALSED emissivity image of the Central Valley in California with Fresno to

521   the west and Sequoia National Park to the east over the Sierra Nevadas. The image was

522   computed using histogram-equalization and plotting ASTER emissivity in bands 10, 12

523   and 14 as red, green and blue respectively. Bare surfaces with high spectral contrast

524   appear purple to black (Sierra Nevadas), grasslands appear green and yellow (Savannah

525   region), and dense vegetation canopies (redwood forests and cropfields) appear white and

526   light blue in color.

527

528

529
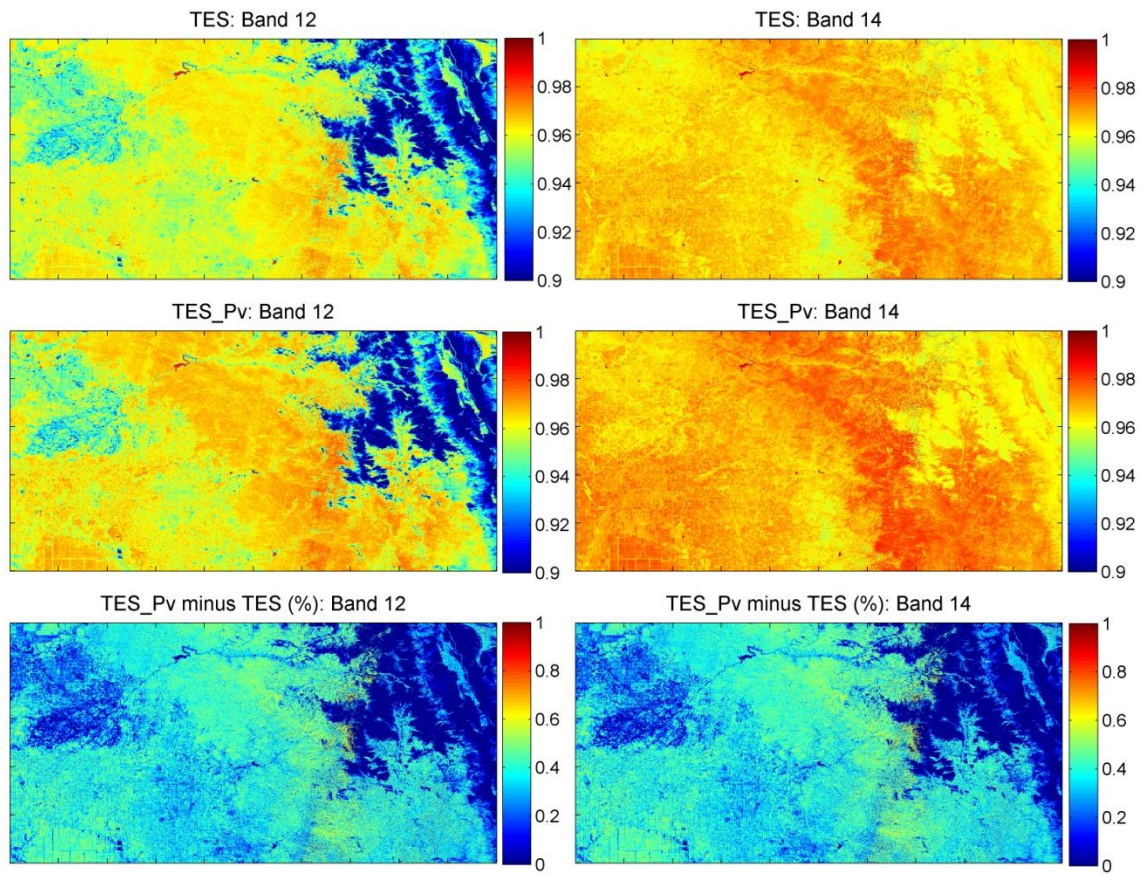
530   Figure 8. Comparisons between TES and TES_Pv emissivity results for band 12 (left

531   panels) and 14 (right panels) for the area in Figure 2. The two bottom panels show the

532   emissivity differences ranging from 0 to 1% in bands 12 and 14.
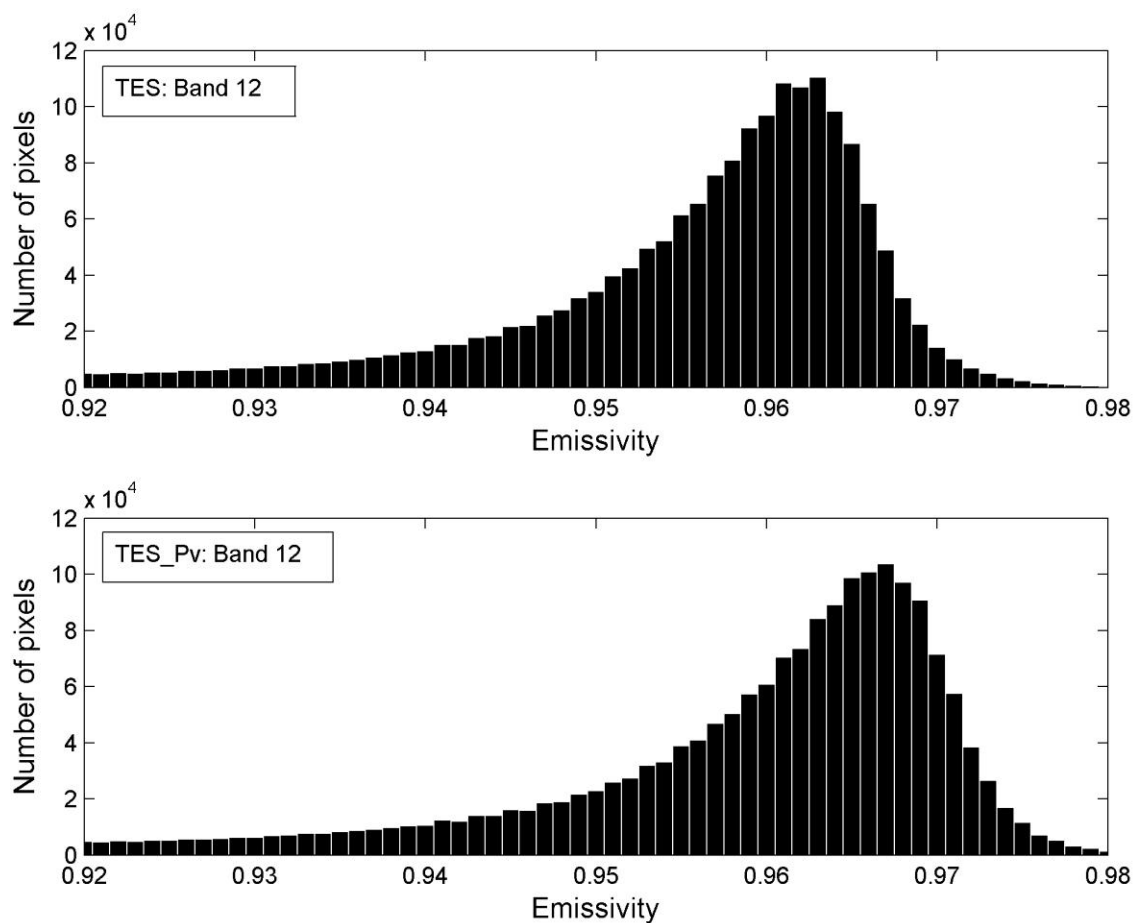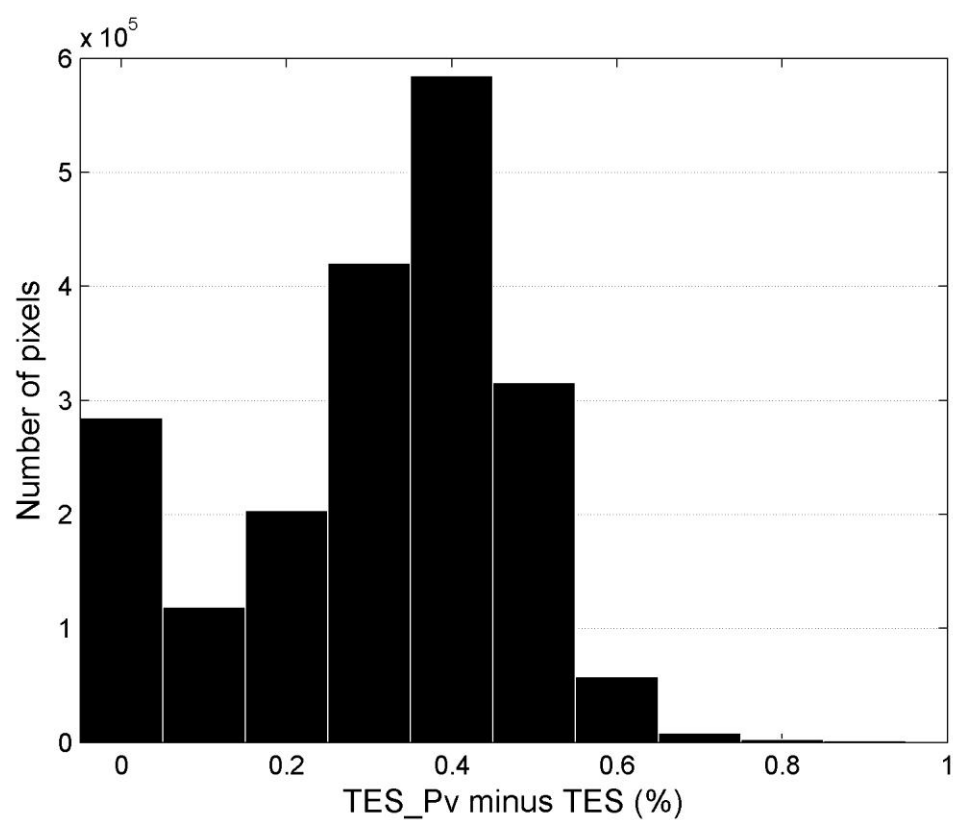
533

534

535   Figure 9. Histogram showing the emissivity variation above 0.92 for TES (top panel) and

536   TES_Pv (bottom panel) using 2 million ASTER pixels from Figure 2.

537

538

Figure 10. Histogram of the emissivity difference between TES and TES_Pv using 2
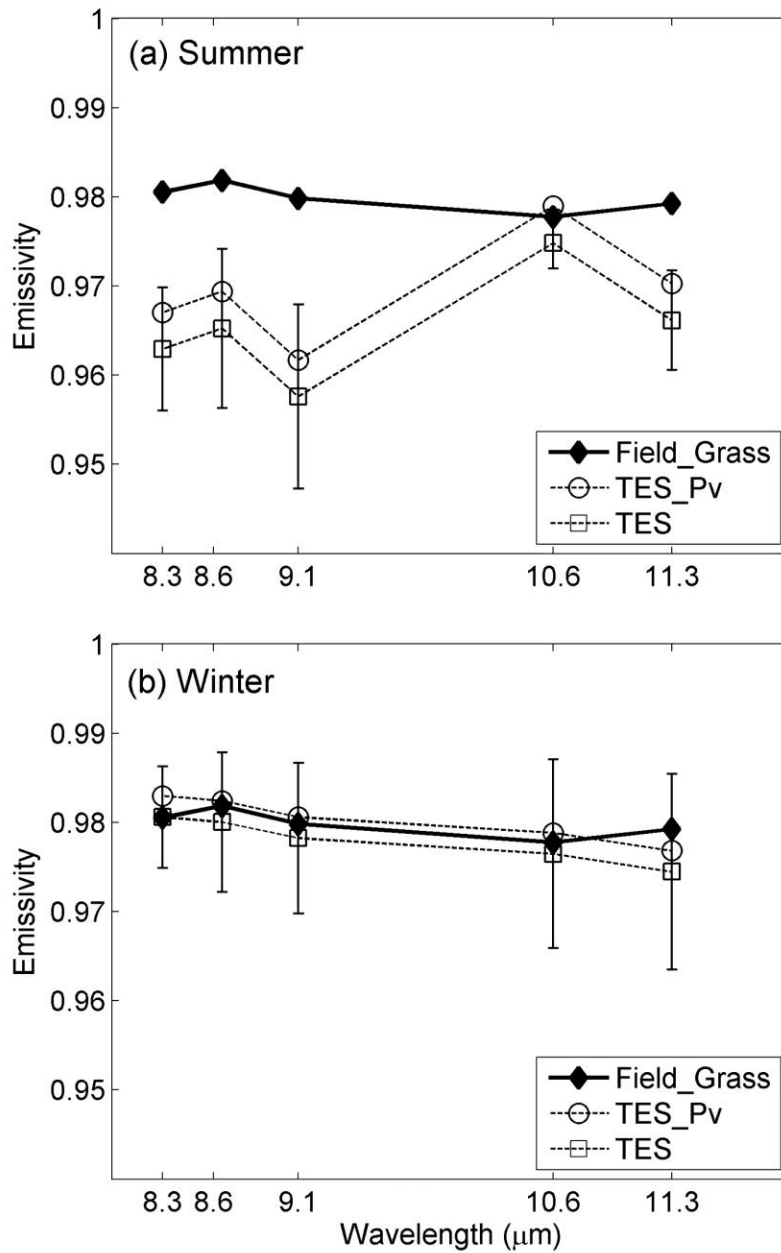
million ASTER pixels from Figure 2.

541

Figure 11. Emissivity spectra of the new TES_Pv, original TES, and sun-shadow method

over a grassland in Dallam County, Texas for (a) Summer and (b) Winter NAALSED

observations. The sun-shadow field measurements were convolved to the appropriate

ASTER spectral response functions.